

Flame dynamics of an injection element operated with LOX/H₂ and LOX/CNG in a high-pressure rocket combustor with large optical access

Jan Martin^{★†}, Wolfgang Armbruster[★], Robert Stützer[★], Dmitry Suslov[★], Justin Hardi[★],
Michael Oswald^{★‡}

[★]DLR, Institute of Space Propulsion, 74239, Hardthausen am Kocher, Germany
Im Langen Grund, 74239, Hardthausen am Kocher, Germany

[‡]RWTH Aachen University, Institute of Jet Propulsion and Turbomachinery
Templergraben 55, 52062, Aachen, Germany

jan.martin@dlr.de · wolfgang.armbruster@dlr.de · robert.stuetzer@dlr.de · dmitry.suslov@dlr.de · justin.hardi@dlr.de ·
michael.oschwald@dlr.de

[†]Corresponding author

Abstract

Hot fire tests were performed with a single-injector research combustor featuring a large optical access window (255x38 mm) for flame visualisation. Three test campaigns were conducted with the propellant combination of liquid oxygen and hydrogen (LOX/H₂), liquid oxygen and compressed natural gas (LOX/CNG), and liquid oxygen and liquefied natural gas (LOX/LNG) at conditions relevant for main- and upper-stage rocket engines. The large optical access enabled synchronized flame imaging using ultra-violet (OH*) and blue (CH*) radiation wavelengths covering a large portion of the combustion chamber for various sets of sub- and supercritical operating conditions. Combined with temperature, pressure and unsteady pressure measurements, this data provides a high-quality basis for validation of numerical modeling. Flame width, length and opening angle as features describing the flame topology were extracted from the imaging. Two-dimensional distributions of Rayleigh index were calculated for acoustically unexcited and excited hot-fire intervals. These Rayleigh Index values properly reflect the thermoacoustic state of the chamber.

1. Introduction

Liquid propellant rocket engines (LPREs) are a key technology for space launchers world wide. The liquid oxygen-hydrogen (LOX/H₂) propellant combination offers the highest specific impulse under all flown chemical propellants.^{10,25} The European Ariane 5 and Ariane 6 rely on LOX/H₂ rocket engines, and other recent examples include the Japanese LE-9,¹¹ the Russian RD-0146,¹⁹ the Chinese YF-77,²⁷ and in the US, the RS-25 for the Space Launch System, the RL-10C, and the BE-3. The liquid-oxygen/methane (LOX/CH₄) combination is predicted to be cheaper and easier to handle than LOX/H₂ and thus there is growing interest in these propellants. Examples of LOX/CH₄ engines currently in development are the Japanese LE-8,¹ the Chinese TQ-11 and TQ-12, the European Prometheus²³ and M-10, and the Raptor and BE-4 in the US.

Due to its direct influence on flame anchoring, combustion stability, system pressure and overall performance the injector design is a crucial element in the development of LPREs. The velocity ratio ($VR = u_f/u_o$) and the momentum flux ratio ($J = \rho_f u_f^2 / \rho_o u_o^2$) are non-dimensional numbers describing the shear forces from the velocity difference of the injected propellants and thus the atomization and mixing. Therefore, they often serve as important design parameters governing the combustion efficiency of an engine.²⁸ Often the injectors are placed in sub-scale experiments to verify the desired performance before implementing into full-scale engines.^{14,15,17,21,24} Such experiments can also serve test cases to validate CFD tools for use in the design process.

Sub-scale experiments can also be used to assess the thermoacoustic stability characteristics of a particular injector design.^{6,9} Thermoacoustic instabilities are the coupling of oscillating heat release rate (\dot{q}') with pressure oscillations (p') in the combustion chamber. Instabilities can arise if the Rayleigh criterion is satisfied, which can be expressed as

$$\int_0^T \int_V p'(\vec{x}, t) \dot{q}'(\vec{x}, t) dV dt > 0. \quad (1)$$

FLAME DYNAMICS OF LOX/HYDROGEN AND LOX/METHANE COMBUSTION

Measuring p' at the wall of a combustion chamber is relatively straight forward, whereas \dot{q}' cannot be measured directly. In former studies, ultraviolet radiation measurements in the band corresponding to the hydroxyl radical (OH*) have often been used as a marker for heat release rate in sub-scale experiments.^{2,8,20} The interpretation of such measurements can be complicated by the fact that OH* radiation suffers from high self-absorption at pressures relevant for most engines, resulting in the measured intensities dominated by the emission closest to the observer. Furthermore, at temperatures above 2700 K, OH* emission is dominated by thermal excitation rather than chemiluminescence preventing a direct relation between intensity and \dot{q}' . In contrast, radiation in the blue wavelengths, for example in the band corresponding to CH* emission, can be considered optically thin under such conditions and can complement OH* measurements for the assessment of combustion dynamics.^{8,17} Although lacking an established proportionality between line-of-sight integrated radiation measurements and \dot{q}' , the correlation of intensity with pressure can give a qualitative indication of the thermoacoustic interaction.

A more straightforward approach to assessing the Rayleigh criterion is the direct extraction of \dot{q}' from simulations, which again emphasizes the need for high-quality validation data. In addition to global parameters such as combustion chamber pressure and mass flow rates, detailed information concerning flow parameters and boundary conditions are necessary to validate that the injection, atomization, and combustion processes are captured correctly. Hence there is a need for suitable experimental data.^{13,24} Here sub-scale combustion chambers play a special role because they can accommodate optical access and provide spatially resolved radiation measurements as a valuable point of comparison with numerical results.

The DLR optically accessible rocket combustor model 'N' (BKN) addresses the aforementioned need for validation test cases. The experiment is extensively equipped with conventional diagnostics, such as thermocouples and pressure sensors and is thus able to provide well-defined boundary conditions. The large optical access window enables the examination of a great portion of the flame, providing information on the steady-state flame topology as well as thermoacoustic interaction under different sets of operating conditions. This work presents experiments with BKN and the propellant combination of LOX and compressed-/liquefied-natural-gas (CNG/LNG) and a comparison with previous experiments with the same injection element but hydrogen H_2 as the fuel. In the tests with hydrocarbon fuel, high-speed imaging of OH* and CH* radiation was conducted. While there is no formation of CH* in LOX/ H_2 combustion, the same optical filter for CH* was used in the H_2 tests to capture the blue radiation (BR) in the same wavelength range.

First, the experimental setup including the optical diagnostics and operating conditions will be presented for the latest experiments with LOX/LNG. Then, the methodology of the performed analysis will be described. The influence of three LOX/LNG operating conditions on the flame topology will be shown and discussed in comparison to previous LOX/CNG and LOX/ H_2 experiments. Finally, the flame response during intervals of heightened acoustic excitation of the first longitudinal resonance frequency (1L mode) of the chamber will be compared to non-excited intervals.

2. Experimental Method

2.1 Combustion Chamber

The hot-fire tests with BKN presented in this work were conducted at the European Research and Technology Test Facility P8⁷ for cryogenic rocket engines. The experimental hardware consists of a single-element injector head, an optical combustion chamber segment with 50 mm diameter, additional chamber segments, and a convergent divergent nozzle with a throat diameter (d_t) of 14.5 mm. This results in an overall length (l_{cc}) from injection plane to nozzle throat of 539 mm for the subcritical and 609 mm for the supercritical load points. The geometry of the inner surface of the optical access window matches the contour of the combustion chamber wall to minimize disturbance to the symmetry of the flow field in the combustion chamber.¹⁷ The schematic of the combustor configuration is illustrated in Fig.1.

In order to provide an extensive set of boundary conditions, at least one temperature, static pressure and unsteady pressure measurement is made in the manifolds for LOX (T_o, P_o, p'_o), LNG (T_f, P_f, p'_f), and window cooling (T_c, P_c, p'_c). 13 thermocouples ($T_{cc,1-13}$) in the combustion chamber protrude approximately 0.1 mm into the chamber and are distributed every 20 mm between 4.5 mm and 244.5 mm downstream of the injection plane. An additional 12 thermocouples ($T_{ccs,1-12}$) are mounted within the chamber walls with contact to the structure, 1 mm back from the combustion chamber wall and also placed every 20 mm between 34.5 mm and 254.5 mm downstream of the faceplate. Static pressure sensors ($P_{cc,1-13}$) sampled at a rate of 100 Hz are connected to the chamber at the same axial positions as $T_{cc,1-13}$. For acoustic measurements, six flush mounted, unsteady pressure sensors are positioned at distances of 34.5 mm, 84.5 mm, 94.5 mm, 134.5 mm, 164.5 mm and 234.5 mm downstream of the faceplate, and one recessed sensor is at 367 mm. The signals are sampled at a rate of 100 kHz and have a measurement range of ± 30 bar.

LOX and LNG are injected through a shear coaxial injection element with a tapered LOX post. Film cooling with CNG reducing the heat load to the optical windows is injected via an annular gap between chamber wall and

FLAME DYNAMICS OF LOX/HYDROGEN AND LOX/METHANE COMBUSTION

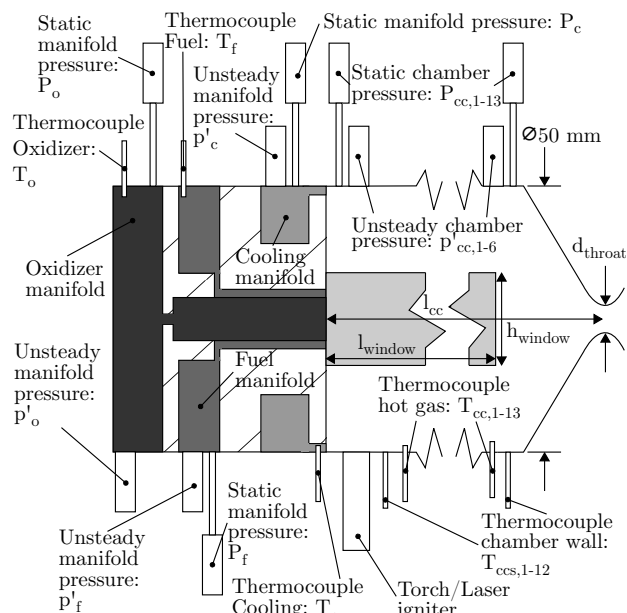
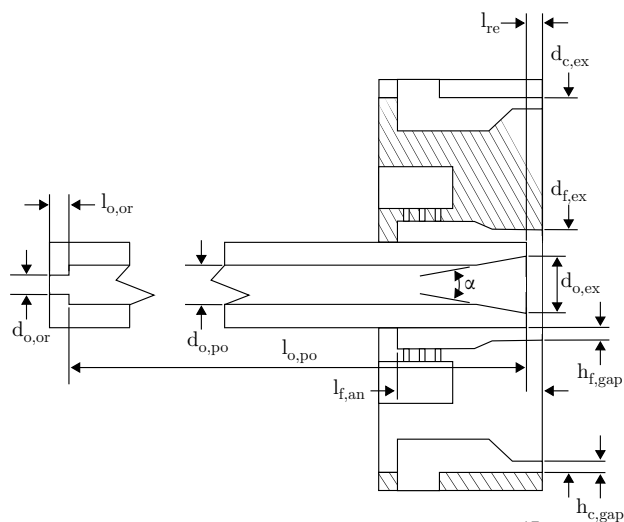


Figure 1: Experimental combustor model 'N' (BKN) configuration

Figure 2: Injection system configuration¹⁷

faceplate. Both injection systems are illustrated in Fig. 2. The dimensions of the injection system are given in Table 1.

2.2 Optical Setup

Visualization of the flame with UV and BR was carried out using two synchronously and coaxially recording high-speed camera systems. The UV regime is dominated by the intense radiation from the OH* radical with its intense emission bands around 310 nm. The excited H₂O₂ molecule with its broad spectral continuum around 450 nm⁴ is believed to strongly contribute to the BR. For hydrocarbon combustion the methylidyne radical (CH*) radiating at 436 nm³ plays the dominant role. The optical axis was split by a dichroic mirror (transparent for visible light and reflective for UV radiation) in order to obtain an identical field of view for both camera systems.

The blue flame emission was recorded by a Photron® Fastcam SA-Z type 2100K-M-64G camera model. Its proprietary design advanced CMOS image sensor has an active area of 20.48 × 20.48 mm, and 1024 × 1024 pixels respectively. The RAM capacity of 64GB allows the storage of 43,682 frames at full resolution. Flame emission, without background illumination, was recorded with 7,200 fps – 20,000 fps and exposure times of 16 – 30 μs. A Carl Zeiss® Makro-Planar ZF.2 lens with f=100 mm and an aperture of 3.5 was used, equipped with a band pass filter (CWL: 436 nm; FWHM: 10 nm; T(436 nm): 50%) from Andover Corporation.

UV radiation (OH*) was recorded using an image intensified Photron® Fastcam SA-X2 type 480K-M4 high-

FLAME DYNAMICS OF LOX/HYDROGEN AND LOX/METHANE COMBUSTION

Table 1: Geometrical dimensions of injection systems

Symbol	$d_{o,or}$	$l_{o,or}$	$d_{o,po}$	$l_{o,po}$
Unit	mm	mm	mm	mm
Value	2.2	4.0	5.5	127.0
Symbol	$d_{o,ex}$	α	$l_{f,an}$	$d_{f,ex}$
Unit	mm	°	mm	mm
Value	6.3	8	34.5	8.2
Symbol	$h_{f,gap}$	$d_{c,ex}$	$h_{c,gap}$	l_{re}
Unit	mm	mm	mm	mm
Value	0.5	50.0	0.4	4.0

Table 2: Steady state and injection conditions for both load points

Parameter	Unit	Load point				Uncertainty
		1	2	3	4	
P_{cc}	bar	62.9	65.4	41.3	40.5	$\pm 1.1\%$
ROF		3.5	3.0	3.4	2.5	$\pm 5\%$
\dot{m}_o	kg/s	0.358	0.355	0.228	0.215	$\pm 3\%$
\dot{m}_f	kg/s	0.103	0.117	0.068	0.088	$\pm 3\%$
\dot{m}_c	kg/s	0.338	0.355	0.212	0.208	$\pm 3\%$
T_o	K	104	106	105	109	$\pm 3.5 K$
T_f	K	217	216	192	255	$\pm 3.5 K$
T_c	K	281	283	271	270	$\pm 2.0 K$

speed camera, also equipped with an identical proprietary design advanced CMOS image sensor. Frame rates of 7,200 Hz – 20,000 Hz were applied. The UV radiation was converted into visible light using a Hamamatsu® image intensifier, model C10880 GHD1101, which was attached to the camera’s lens mount. Gate width and gain were set for optimal image quality. A Nikon® UV-Nikkor f=105 mm lens with an aperture of 4.5 was used, equipped with a UV band pass filter (CWL: 306.8 nm; FWHM: 10 nm; T(306.8 nm): 64%).

2.3 Operating Conditions

In the campaign with BKN and the propellant combination LOX/LNG, tests were conducted at chamber pressures from 41 up to 66 bar and ROFs at the main injector between 2.5 and 3.5. Data of three load points (LPs) originating from two different test runs are presented in this work.

The test runs are presented in Fig.3. The test sequences are described with traces of the static chamber pressure P_{cc} , LOX injection temperature T_o , mixed CNG and LNG injection temperature T_f , and ratio of oxidizer to fuel mass flow rate ROF (bottom). These traces of parameters describe the performed sequence of operating conditions, while the raw unsteady pressure signal (middle) and the spectrogram (top) describe the acoustic character. The duration of each LP is about 0.5 s respectively 0.3 s for LP4. This allows a steady-state thermal equilibrium condition to be reached. The intervals used for extracting the data of LP1 and LP2 (16.5-17.0 and 19.0-19.5 s in the first test) and LP3 and LP4 (15.9-16.4 4.9-5.2 in the second test) are highlighted in gray. High-speed imaging of OH* and CH* with 13.5 kfps for LP1 and LP2 and 20 kfps for LP3 and LP4 is available.

Both test runs develop high amplitude combustion instabilities characterized by excitation of the chamber longitudinal resonance modes. Table 2 summarizes the steady state test condition and the injections condition for both load points. The data are mean values from a sample period of 0.5/0.3 s.

3. Methodology

3.1 Flame topology analysis

The flame opening angle, the flame width and the flame length were measured within the framework of the flame topology analysis. For the flame opening angle a threshold based flame boundary detection algorithm¹⁷ was applied to a time averaged image of the corresponding LP. A linear fit to the boundaries of the detected flame was performed in the first 6 % of the flames’ optically accessible length, which enabled the derivation of an flame opening angle. For the

FLAME DYNAMICS OF LOX/HYDROGEN AND LOX/METHANE COMBUSTION

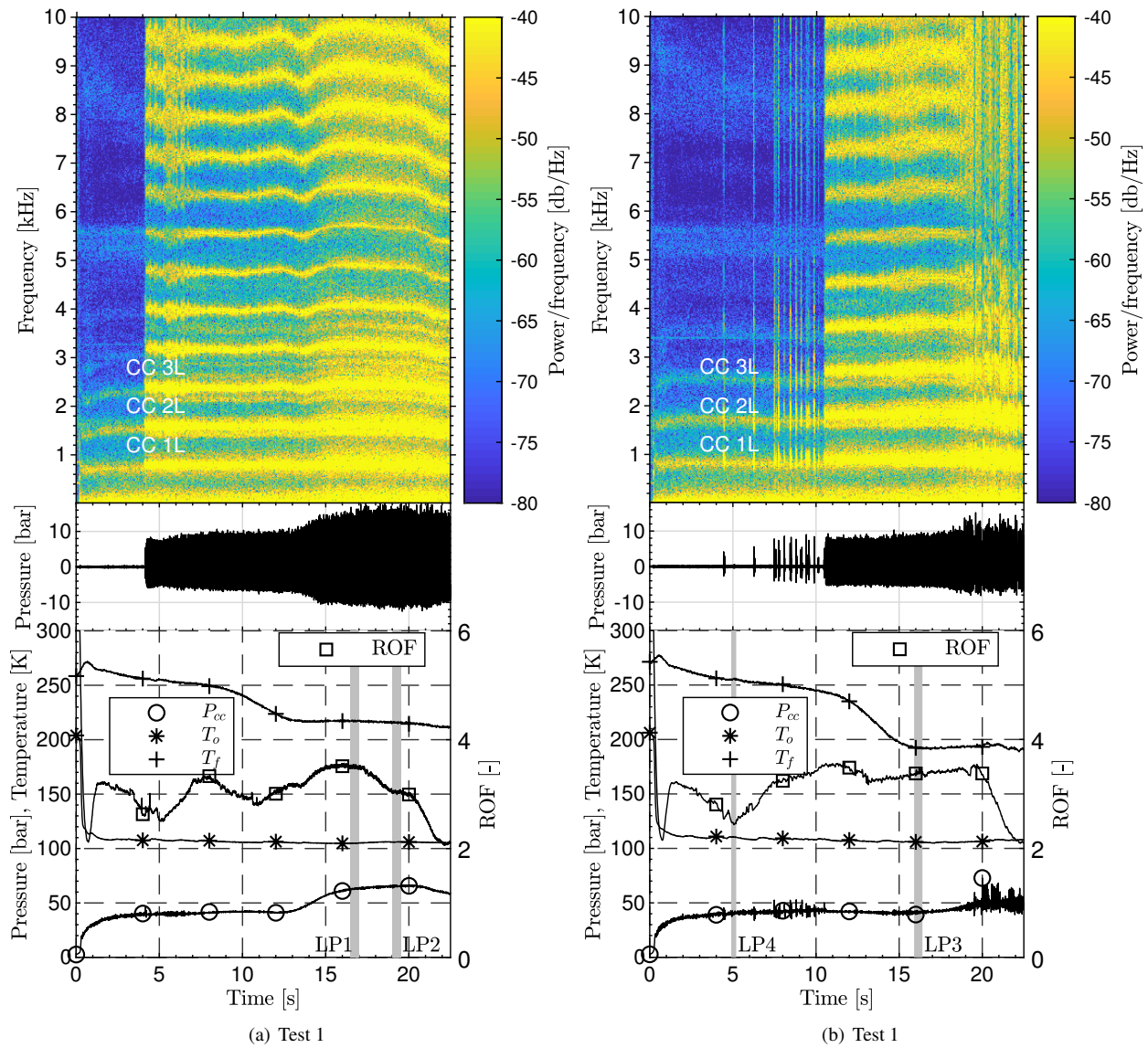


Figure 3: Sequence of tests with operating conditions and gray highlighted interval used for extracting the data for all load points

FLAME DYNAMICS OF LOX/HYDROGEN AND LOX/METHANE COMBUSTION

determination of the flame width, mean values of each row and for the flame length mean values of each column were calculated. In this case, 75% of the peak intensity from the time averaged OH* and blue radiation images was used to define the flame width at three quarter maximum (FIW34M) and the flame length at three quarter maximum (FIL34M). It should be noted that for the latter case only the downstream limitation of the intensity at three quarter maximum has been considered.

3.2 Flame dynamics analysis

The dynamic mode decomposition (DMD) was applied to isolate the underlying dynamics in the data with respect to its frequencies. The slightly adapted implementation of a multi-variable DMD² enables a direct analysis of the high-speed imaging in relation to measurements from various sensors. Therefore, the sensor data is resampled to the snapshots of high-speed imaging and added as pseudo-pixels to the input matrix of the DMD algorithm. The algorithm decomposes the data into three matrices. One containing the spatial data, the second containing the amplitudes and the third the temporal data of each mode. The matrix containing the spatial data of each mode is divided again in the imaging and sensor data. Thus each type of measurement can be treated individually but is filtered to modes containing the same frequency content.

The decomposed pressure oscillations gained from the DMD can be compared to bandpass filtered data with a narrow filter width and are used to reconstruct the pressure field in the chamber. The 1D-pressure distribution in the window region is interpolated by a spline-interpolation method. Combining both (intensity and pressure) reconstructions, a 2D Rayleigh-Index via Eq. 2 for each (or multiple) frequencies referring to the decomposed mode(s) m can be calculated.

$$RI(x, r) = \sum_m (|p'(x, r, f(m))||I'(x, r, f(m))| \cos(\Theta_{p'-I'}(x, r, f(m)))) \quad (2)$$

Here I' denotes the fluctuating part of the captured intensity, p' the pressure oscillations and $\Theta_{p'-I'}$ the phase difference (according to Eq. 3) between those signals for each pixel in dependency of the reconstructed mode and thus the frequency.

$$\Theta_{p'-I'}(x, r, f(m)) = \Theta_{p'(x,r,f(m))} - \Theta_{I'(x,r,f(m))} \quad (3)$$

4. Results

4.1 Flame characteristics

First the flame visualizations will be shown for the four LPs with the propellant combination of LOX/LNG. The instantaneous flame radiation measurements of the first recorded frame in each LP (Figs.4(a)-4(d)) and the time-averaged flame visualization over the whole duration of each LP (Figs.5(a)-5(d)) show the OH* imaging on the top and the CH* imaging at the bottom. The CH* radiation displays the same half of the flame as the OH* radiation but mirrored.

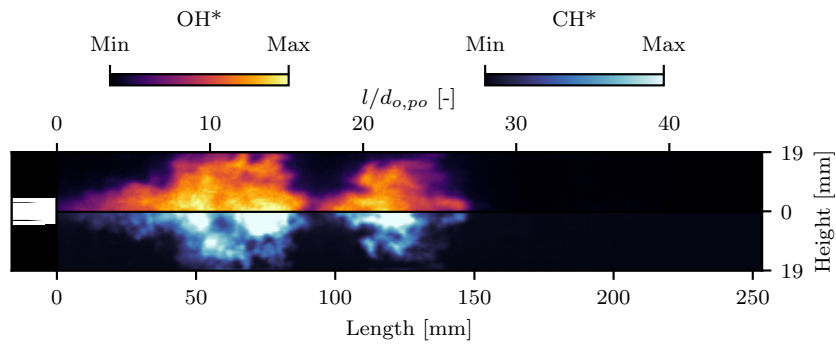
The first three LPs are dominated by high-amplitude longitudinal combustion instabilities. This is reflected in the flame radiation imaging, with the high-speed image sequences describing a violent longitudinal pulsation of the flame, undergoing stretching and compression due to entrainment in the acoustic velocity field. The instantaneous snapshots show a significantly shortened flame compared to stable conditions in LP4. Moreover, the flames are interrupted through their pulsating motion, being pinched and separating into large pockets of combusting propellants from around 60-90 mm downstream.

The time-averaged flame images of the three unstable LPs (Figs.5(a)-5(c)) also show the shortened flame in comparison to LP4 (Fig.5(d)). The average images for LP3 and LP4 (Fig.5(c)/Fig.5(d)) suffer regions of reduced intensity within the flame around 90-140 mm downstream due to soot deposition onto the surface of the quartz window. The soot contamination affects the CH* radiation intensity more than OH*.

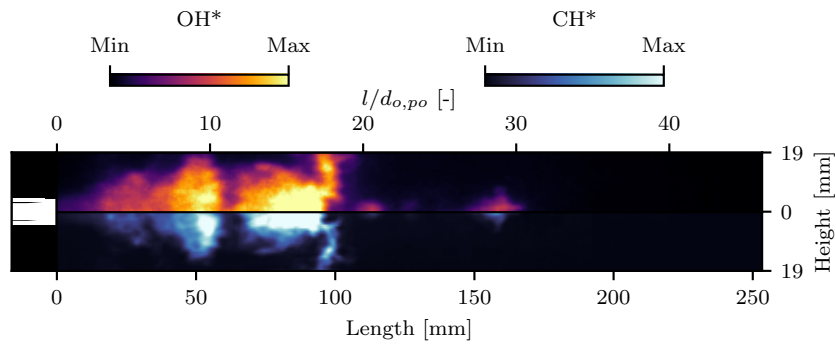
The hot gas temperature and the structural temperature measurements also reflect the shortened flame revealed by the flame imaging. For the hot gas temperatures in Fig. 6(a), a steep rise of the measured values is noticeable in the first 100 mm of the chamber, followed by a decrease from approximately 150 mm. Due to the high-amplitude instabilities accompanied high temperatures within the chamber the thermocouples at 84.5 mm, 104.5 and 144.5 mm were damaged during the first test including LP1 and LP2 and thus no measurements are available.

The structural temperatures also reach their peak by around 100 mm, as seen in Fig. 6(b). However there is no monotonic decrease after 150 mm as in the gas temperature distribution. The thermocouple at 170 mm was damaged and can be neglected in this plot.

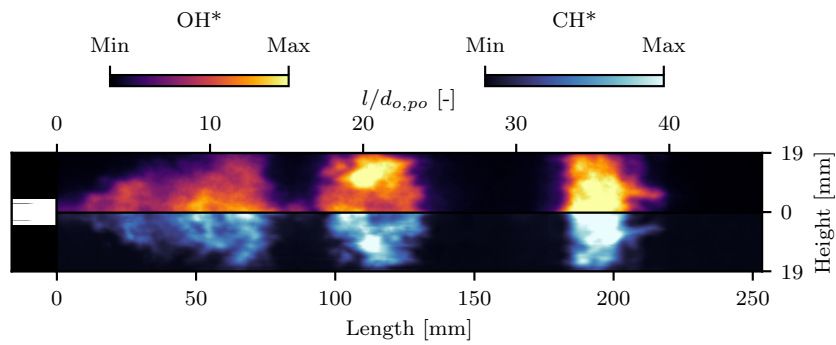
FLAME DYNAMICS OF LOX/HYDROGEN AND LOX/METHANE COMBUSTION



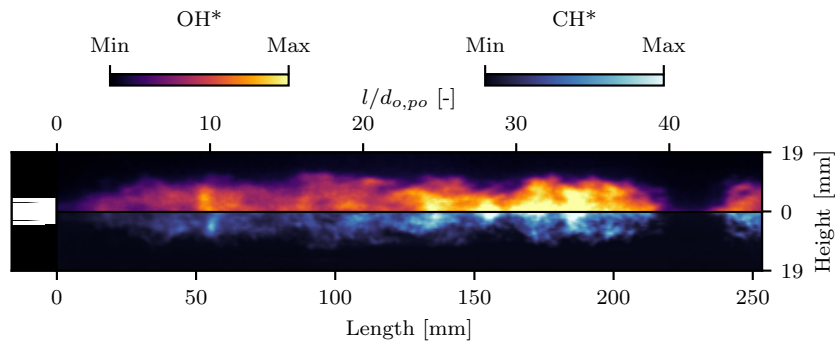
(a) LP1



(b) LP2



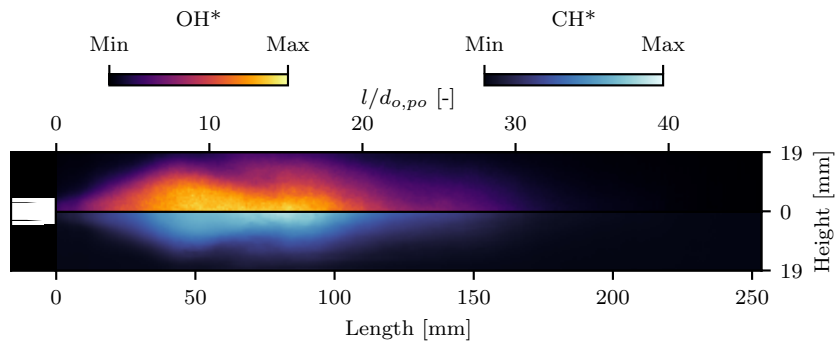
(c) LP3



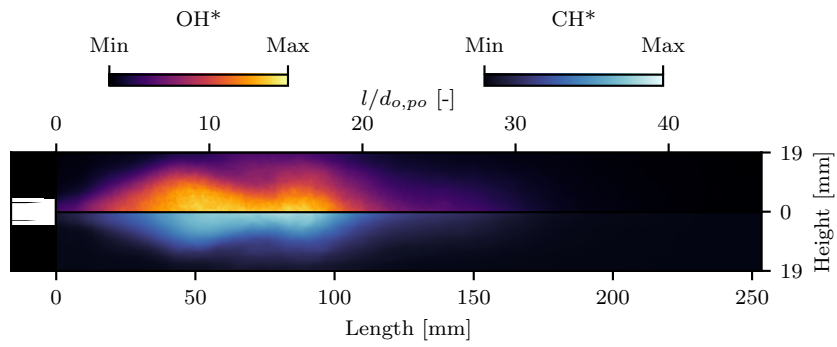
(d) LP4

Figure 4: Instantaneous flame radiation imaging (OH*/CH*)

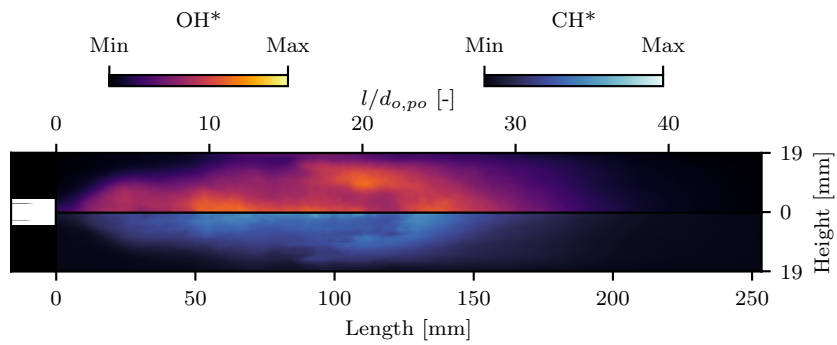
FLAME DYNAMICS OF LOX/HYDROGEN AND LOX/METHANE COMBUSTION



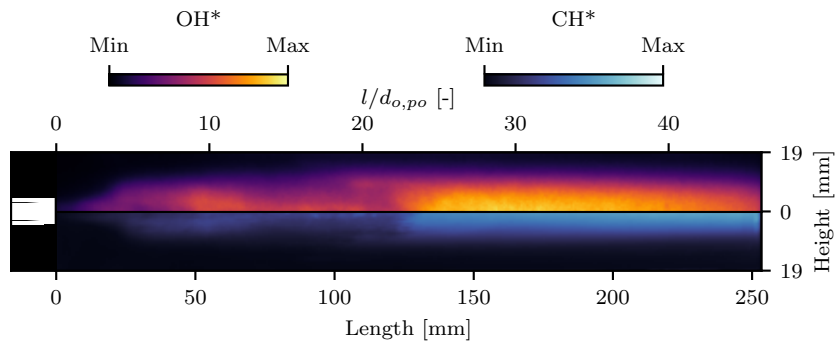
(a) LP1



(b) LP2



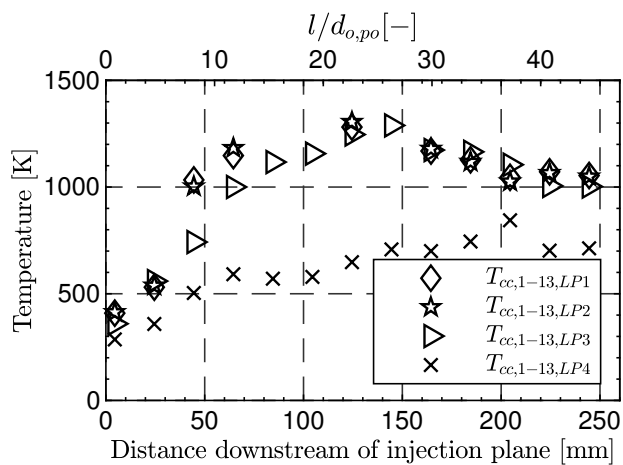
(c) LP3



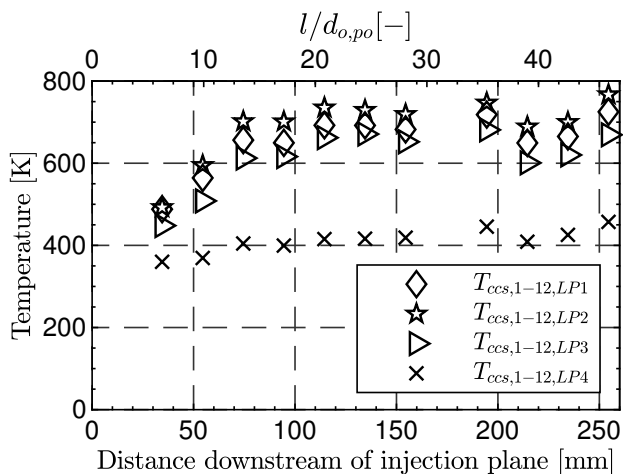
(d) LP4

Figure 5: Time-averaged flame radiation imaging (OH*/CH*)

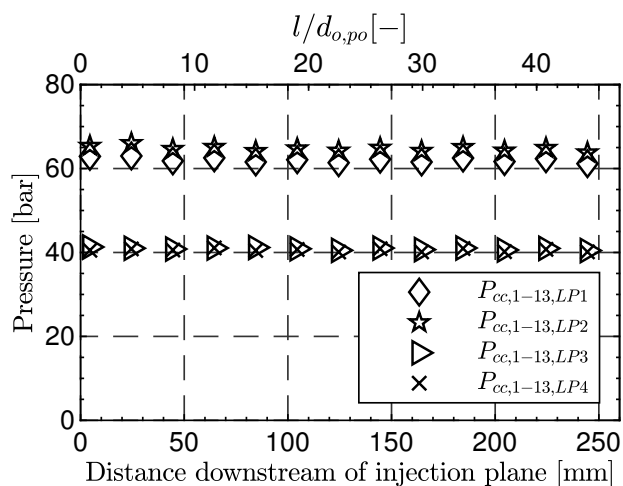
FLAME DYNAMICS OF LOX/HYDROGEN AND LOX/METHANE COMBUSTION



(a) Hot gas temperature



(b) Wall temperature

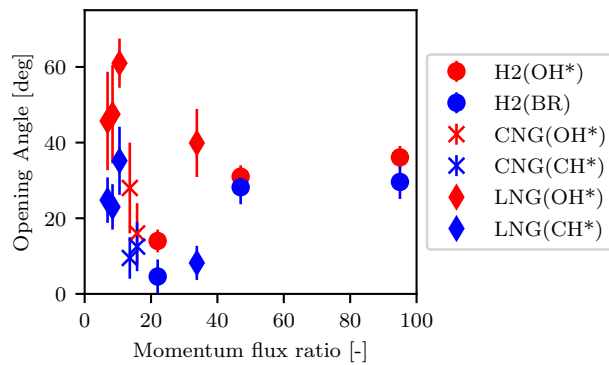


(c) Pressure

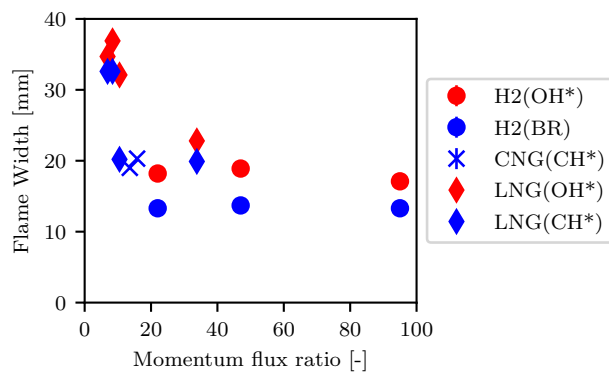
Figure 6: Axial development of conventional measurements

FLAME DYNAMICS OF LOX/HYDROGEN AND LOX/METHANE COMBUSTION

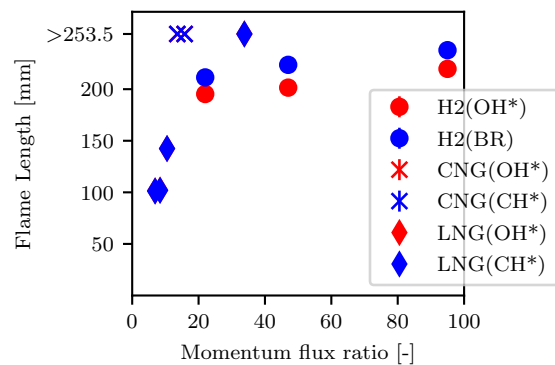
The pressure measurements in Fig. 6(c) show only a slight decrease towards the end of the optical segment. This is to be expected due to the long chamber length and high contraction ratio (ϵ_c) of the nozzle.



(a) Flame opening angle



(b) Flame width



(c) Flame length

Figure 7: Flame characteristics in correlation to momentum flux ratio

In the next step further flame characteristics, flame opening angle, width, and length of the presented LPs with the propellants of LOX/LNG will be compared to LPs in previous test campaigns with the same combustion chamber and injection element, but with LOX/H₂ and LOX/CNG. A precise description of these LPs can be found in previous publications focusing on the tests with LOX/H₂¹⁷ and LOX/CNG.¹⁸ All parameters have been derived from the time-averaged flame imaging of each LP.

The flame opening angles, plotted in Fig. 7(a), follow the expected trend of higher opening angles due to the increased shear forces with higher value of VR and J and thus improved mixing,^{12,17} regardless of the fuel. The exception are the values from the unstable LPs in the LNG campaign, which can be explained by the strong combustion instabilities causing the opening angle to vary dynamically and be generally increased by the upstream compression of the flame by the acoustic oscillations. The dynamic pulsation in the near injector region also responsible for the large uncertainty in these measurements. The same applies for the outlying OH* measurements in the tests with CNG. The

FLAME DYNAMICS OF LOX/HYDROGEN AND LOX/METHANE COMBUSTION

increased angles and heightened uncertainty also reflect fluctuations in the near injector region. It can also be seen that for the LNG campaign the spread between the extracted angle based upon the CH^* and OH^* radiation is increased.

The flame width values plotted in Fig. 7(b) are relatively constant for the stable and semi-stable operating conditions with H_2 and CNG as fuel. Perhaps the tests with natural gas as fuel tend to feature higher values. Again the unstable LPs of the LNG campaign result in considerably higher values for the flame width. The outlying flame width value of approximately 20 mm based upon the CH^* measurement with LNG as fuel is compromised by the contamination of the quartz glass as discussed with respect to Fig. 5(c).

Flame length measurements are plotted in Fig. 7(c). While for the LOX/H_2 experiments the flame length ranged between 190 and 240 mm, no decrease of the intensity was detectable for the CNG tests and the LNG LP4 with stable conditions and thus a flame longer than the optical accessible length of the window (253.5 mm) was assumed. The unstable LPs with LNG feature a flame with nearly half of the length compared to previous tests due to the previously discussed flame dynamics.

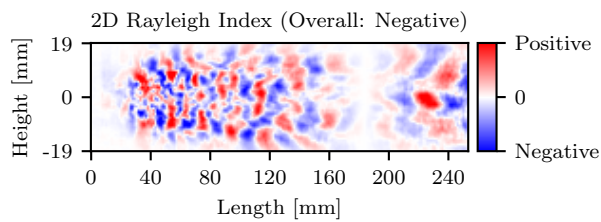


Figure 8: Rayleigh index distribution at the chamber 1L frequency for LOX/H_2 LP (1, H_2).¹⁶

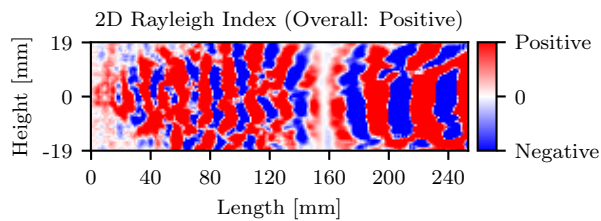


Figure 9: Rayleigh index distribution at the chamber 1L frequency for an excited interval of a LOX/CNG LP (1, CNG).¹⁸

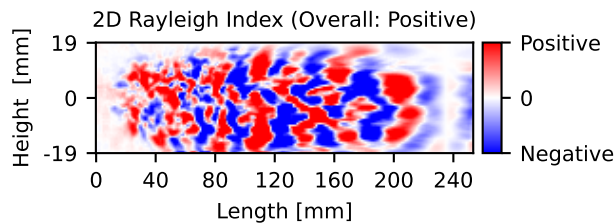


Figure 10: Rayleigh index distribution at the chamber 1L frequency for LP4.

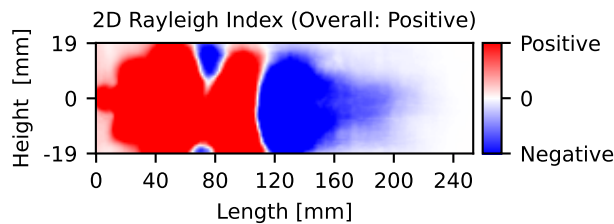


Figure 11: Rayleigh index distribution at the chamber 1L frequency for LP1.

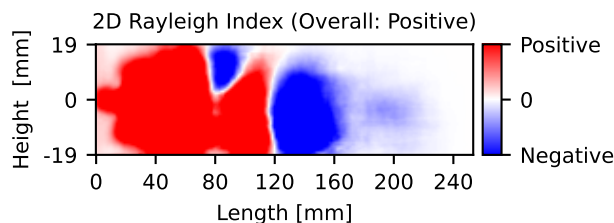


Figure 12: Rayleigh index distribution at the chamber 1L frequency for LP2.

FLAME DYNAMICS OF LOX/HYDROGEN AND LOX/METHANE COMBUSTION

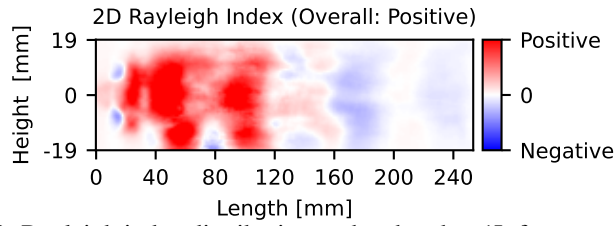


Figure 13: Rayleigh index distribution at the chamber 1L frequency for LP3.

4.2 Flame Response

The flame response in form of calculated 2D Rayleigh indices according to Eq.2 will now be presented. Given that the BR (including CH* for CNG/LNG fuel) has a greater depth of view,⁵ more information about the integral rate of heat release is contained in this measurement. Therefore the BR measurements were used to calculate the Rayleigh indices. Within the index distributions, positive (red) values means that the acoustic and intensity oscillations are in phase, while negative (blue) regions show counter-phased dynamics.

Figure 8 visualizes the flame response for an unexcited LOX/H₂ LP (2,H₂). Here, alternating small red and blue structures can be seen. These describe the downstream translation of small turbulent structures on the flame surface. The overall Rayleigh index, integrated over the whole window region, is negative. Thus no major interaction between the acoustic field and the flame are taking place.

This is not the case for the excited interval of the LOX/CNG LP (1,CNG) in Fig. 9. Here, the overall index is slightly positive. Furthermore, the regions in which the flame couples with the acoustic field form larger (red) structures. The near injector region is known to have a major influence on stability behavior of combustion chambers with shear coaxial injectors,^{22,26} and this region is dominated by positive coupling. A similar but weaker behavior can be seen for the stable LNG LP4 (Fig. 10). Finally, the index distributions of the three unstable LNG LPs are shown in Figs. 11-13, and draw a different picture. In addition to a strongly positive overall index, it can be clearly seen that nearly the whole flame zone is positively coupled with the acoustic pressure oscillations.

Table 3 summarizes the integrated Rayleigh-Index in the first 60 mm of the chamber and compares these values to the acoustic amplitude of $p'_{cc,1}$ (located at 34.5 mm) normalized by the mean chamber pressure (P_{cc}) for the tests with LOX/H₂,^{16,17} LOX/CNG¹⁸ and LOX/LNG. The calculated 2D-Rayleigh-Indices reflect the level of thermoacoustic excitation within the chamber consistently. Higher values of overall Rayleigh index from the first 60 mm are associated with higher normalized acoustic pressure oscillations. This correlation is also illustrated in Fig. 14.

Table 3: Acoustic amplitudes and integrated Rayleigh-Index with respect to each LP

Load Point	1,H2	2,H2	3,H2	1,CNG	1,CNG	1,LNG	2,LNG	3,LNG	4,LNG
PCC [bar]	64.3	67.6	43.0	66.8	66.8	62.9	65.4	41.3	40.5
ROF [-]	4.0	5.8	3.4	2.8	2.8	3.5	3.0	3.4	2.5
1L Frequency [Hz]	2425	2425	2470	1310	1340	815	806	920	830
Instability	✗	✗	✗	✗	✓/✗	✓	✓	✓	✗
$\frac{p'_{cc,1}}{P_{cc}}$ [%]	0.07	0.1	0.04	0.1	0.4	12.7	11.3	10.4	0.2
$RI(0-60mm, h_{window})$	$-4.3e^{-3}$	$0.2e^{-3}$	$-5.9e^{-3}$	$1.14e^{-1}$	$7.22e^{-1}$	$4.56e^3$	$3.45e^3$	$5.54e^2$	$1.9e^1$

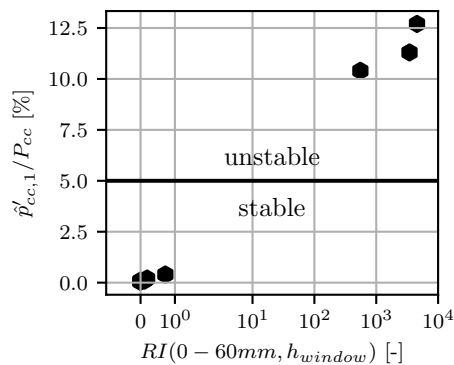


Figure 14: Acoustic amplitude in correlation to the calculated Rayleigh-Indices from Table 3

5. Conclusion

Three different operating conditions of thermoacoustically unstable combustion in an experimental rocket combustor with large optical access using the propellant combination LOX/LNG were presented in this work. The propellants were injected through a shear coaxial injection element. Simultaneous flame radiation imaging of the ultraviolet and blue wavelength ranges was conducted. In combination with the axial development of temperature and pressure signals, well-defined information on the boundary conditions in the combustion chamber is provided and allows the usage of this data set as a test case for validating numerical modeling of LOX/Methane flames.

Features characterizing the flame topology were derived from the time-averaged imaging and compared to previous experiments with the oxidizer-fuel combinations of LOX/CNG and LOX/H₂. Here the major influence of the longitudinal combustion instabilities on the flame opening angle and flame length were evident. While for unstable combustion the flame opening angle was significantly increased, the flame length was nearly half the length of previous more stable tests. This behavior was also reflected in the hot gas and wall temperature measurements within the chamber. The hot gas temperature reached its peak between 100 and 150 mm downstream of the faceplate, corresponding to the end of the shortened flame, and then decreased towards the end of the chamber.

2D Rayleigh index distributions were calculated using the acoustic field reconstructed from unsteady pressure measurements and the high-speed blue radiation measurements. The distributions and integrated values reflect the observed state of thermoacoustic excitation of the chamber. For the three unstable load points, a strong interaction between flame radiation intensity and acoustic pressure oscillations covering nearly the whole flame zone is determined. Comparison to previous experiments with the propellant combinations of LOX/CNG and LOX/H₂ revealed consistent behavior. Higher values of the integrated Rayleigh index accompany higher normalized acoustic pressure amplitude. These data are hoped to serve the community in the validation of numerical tools for the prediction of combustion instability in LOX/LNG rocket engines.

6. Acknowledgments

The work is associated with DLR project of Advanced Methods for reusable Aerospace vehicle DEsign Using artificial intelligence and interdisciplinary numerical Simulation (AMADEUS) and Future Fuels. The authors would also like to thank the crew of the P8 test bench. Special thanks Bernhard Knapp and Stephan General for their support with the optical setup and to Alex Grebe for his assistance in preparing and performing the experiments.

References

- [1] Hiroya Asakawa, Hideaki Nanri, Kenji Aoki, Isao Kubota, Hatsuo Mori, Yasuhiro Ishikawa, Kenichi Kimoto, Shinji Ishihara, and Shinichiro Ishizaki. The status of the research and development of LNG rocket engines in Japan. In *Chemical Rocket Propulsion*, pages 463–487. Springer International Publishing, Aug 2016.
- [2] S. K. Beinke. *Analyses of Flame Response to Acoustic Forcing in a Rocket Combustor*. PhD thesis, The University of Adelaide, Australia, 2017. School of Mechanical Engineering.
- [3] N. Fdida, L. Vingert, G. Ordonneau, A. Ristori, C. Brossard, R. Stützer, and J. Sender. Characterization of a double swirl injector in a LOX/LCH₄ fueled combustor on Mascotte test bench. In *5th European Conference for Aeronautics and Space Sciences*, 2013.
- [4] T. Fiala. *Radiation from High Pressure Hydrogen-Oxygen Flames and its Use in Assessing Rocket Combustion Instability*. PhD thesis, Technical University of Munich, Munich, Germany, 2015.
- [5] T. Fiala, T. Sattelmayer, S. Gröning, J. Hardi, R. Stützer, S. Webster, and M. Oswald. Comparison between excited hydroxyl radical and blue radiation from hydrogen rocket combustion. *Journal of Propulsion and Power*, 33(2):490–500, 2017.
- [6] Tristan L. Fuller. *DYNAMIC COUPLING IN A MODEL ROCKET COMBUSTOR*. PhD thesis, Purdue University, West Lafayette, Indiana, 2019.
- [7] A. Habertzettl, D. Suslov, G. Brümmer, A. Frank, and M. Oswald. European technology test facility for high pressure combustion P8. 20 years research and technology development. In *Deutscher Luft- und Raumfahrtkongress (DLRK) 2016*, Braunschweig, Germany, 2016.

FLAME DYNAMICS OF LOX/HYDROGEN AND LOX/METHANE COMBUSTION

- [8] J. S. Hardi, S. K. Beinke, M. Oswald, and B. B. Dally. Coupling of cryogenic oxygen-hydrogen flames to longitudinal and transverse acoustic instabilities. *Journal of Propulsion and Power*, 30(4):991–1004, 2014.
- [9] Justin S. Hardi, W. Zach Hallum, Cheng Huang, and William E. Anderson. Approaches for comparing numerical simulation of combustion instability and flame imaging. *Journal of Propulsion and Power*, 32(2):279–294, mar 2016.
- [10] Dieter K Huzel and David H Huang. *Modern Engineering for Design of Liquid=Propellant Rocket Engines (Revised and enlarged edition)*. American Institute of Aeronautics and Astronautics, 1992.
- [11] H. Kawashima, T. Kobayashi, and K. Okita. Progress of LE-9 engine development. In *AIAA Propulsion and Energy Forum, 2018 Joint Propulsion Conference*, AIAA 2018-4458, Cincinnati, OH, 2018.
- [12] D Kendrick, G Herding, P Scoufflaire, C Rolon, and S Candel. Effects of a recess on cryogenic flame stabilization. *Combustion and Flame*, 118(3):327–339, aug 1999.
- [13] Knab, O., Riedmann, H., Ivancic, B., Höglauer, C., Frey, M., and Aichner, T. Consequences of modeling demands on numerical rocket thrust chamber flow simulation tools, 2019.
- [14] Ansgar Lechtenberg and Peter M. Gerlinger. Numerical investigation of combustion instabilities in a rocket combustion chamber with supercritical injection using a hybrid rans/les method. In *AIAA Scitech 2020 Forum*.
- [15] Peter C. Ma, Hao Wu, Matthias Ihme, and Jean-Pierre Hickey. Nonadiabatic flamelet formulation for predicting wall heat transfer in rocket engines. *AIAA Journal*, 56(6):2336–2349, 2018.
- [16] Jan Martin, Wolfgang Armbruster, and Justin Hardi. Flame-acoustic interaction in a high-pressure, single-injector, lox/h2 rocket combustor with optical access. In *Symposium on Thermoacoustics in Combustion: Industry meets Academia (SoTiC 2021)*, 2021.
- [17] Jan Martin, Wolfgang Armbruster, Robert StÄ¼tzer, Stephan General, Bernhard Knapp, Dmitry Suslov, and Justin Hardi. Flame characteristics of a high-pressure LOX/h2 rocket combustor with large optical access. *Case Studies in Thermal Engineering*, 28:101546, dec 2021.
- [18] Jan Martin, Wolfgang Armbruster, Dmitry Suslov, Robert StÄ¼tzer, Justin Hardi, and Michael Oswald. Flame characteristics and response of a high-pressure lox/cng rocketcombustor with large optical access. In *33rd International Symposium on Space Technology and Science*, 2022.
- [19] Vladimir Rachuk and N Titkov. The first russian LOX-LH2 expander cycle LRE: RD0146. In *42nd AIAA/ASME/SAE/ASEE Joint Propulsion Conference Exhibit*, AIAA 2006-4904, Sacramento, CA, jul 2006. American Institute of Aeronautics and Astronautics.
- [20] F. Richecoeur, P. Scoufflaire, S. Ducruic, and S. Candel. High-frequency transverse acoustic coupling in a multiple-injector cryogenic combustor. *Journal of Propulsion and Power*, 22(4):790–799, 2006.
- [21] T. Schmitt, G. Staffelbach, S. Ducruic, S. Gröning, J. Hardi, and M. Oswald. Large-eddy simulations of a sub-scale liquid rocket combustor: Influence of fuel injection temperature on thermo-acoustic stability. In *7th European Conference for Aeronautics and Aerospace Sciences (EUCASS) 2017*, Milano, Italy, 2017.
- [22] Moritz Schulze. *Linear Stability Assessment of Cryogenic Rocket Engines*. PhD thesis, Technische UniversitÄ¼t MÄ¼nchen, 2016. Institut fÄ¼r Energietechnik.
- [23] P. SIMONTACCHI, R. BLASI, E. EDELIN, S. SAGNIER, N. RAVIER, A. ESPINOSA-RAMOS, J. BRETEAU, and Ph. ALTENHOEFER. Prometheus: Precursor of new low-ost rocket engine family. 2019.
- [24] Dmitry I. Suslov, Justin S. Hardi, and Michael Oswald. Full=length visualisation of liquid oxygen disintegration in a single injector sub=scale rocket combustor. *Aerospace Science and Technology*, 86:444 – 454, 2019.
- [25] G. P. Sutton and O. Biblarz. *Rocket Propulsion Elements*. John Wiley & Sons, New York, 8 edition, 2010.
- [26] A. Urbano, L. Selle, G. Staffelbach, B. Cuenot, T. Schmitt, S. Ducruix, and S. Candel. Exploration of combustion instability triggering using large eddy simulation of a multiple injector liquid rocket engine. *Combustion and Flame*, 169:129–140, July 2016.

FLAME DYNAMICS OF LOX/HYDROGEN AND LOX/METHANE COMBUSTION

- [27] W. Wang, D. Zheng, and G. Qiao. Development status of the cryogenic oxygen hydrogen YF-77 engine for long-march 5. In *64th International Astronautical Congress (IAC)*, Beijing, China, 2013.
- [28] Seongphil Woo, Jungho Lee, Yeoungmin Han, and Youngbin Yoon. Experimental study of the combustion efficiency in multi-element gas-centered swirl coaxial injectors. *Energies*, 13(22):6055, nov 2020.